Proceedings of the 2006 IEEE International Conference on Robotics and Automation
Orlando, Florida - May 2006

Reality-Based Needle Insertion Simulation for Haptic Feedback in Prostate Brachytherapy *

James T. Hing[†], Ari. D. Brooks[††](MD), Jaydev P. Desai[†a] (PhD)
[†]*Program for Robotics, Intelligent Sensing, and Mechatronics (PRISM) Laboratory*
Drexel University, Philadelphia, PA 19104
[††]*Drexel University College of Medicine, Philadelphia, PA 19104*

Abstract - ***There is a strong need to improve the tools clinicians use for training in procedures such as prostate brachytherapy where the success rate is directly related to the clinician's level of experience. Accurate haptic feedback is needed for developing improved surgical simulators and trainers for such procedures. In prostate brachytherapy, accurate needle placement of radioactive seeds in the prostate is crucial to the success of the surgery and to the quality of life of the patient. Therefore, a trainer or simulator for this and other types of needle insertion tasks require an accurate reality-based quantification and model of the needle and soft tissue interaction. To achieve this, we utilize the x-ray images produced by a dual C-arm fluoroscope setup during a needle insertion task to obtain parameters needed for accurate modeling of soft tissue and needle interactions. The needle and implanted markers in the tissue are tracked during the insertion and withdrawal of the needle at speeds of 1.016mm/sec, 12.7mm/sec and 25.4mm/sec. Both image and force data are utilized to determine important parameters such as the local effective modulus during puncture and the approximate cutting force for soft tissue samples. A finite element model was built using the data to model needle puncture of tissue.***

Index Terms – Surgical simulation, soft-tissue modeling, prostate brachytherapy, cutting force, local effective modulus.

I. INTRODUCTION

Prostate cancer accounts for 31% of cancer incidence and 10% of all cancer related mortality among men in the United States [1]. Among the treatment options for localized prostate therapy, prostate brachytherapy has emerged as an excellent alternative for patients who meet specific criteria because it offers the benefits of a higher gland specific dose of radiation therapy without the side effects of external beam therapy. The goal of implanted seeds for brachytherapy is to maximize the radiation dose to the tumor while minimizing radiation doses to the surrounding tissue such as the rectum, bladder and urethra. Accurate seed positioning is very important to the success of the procedure. Minor deviations in seed alignment caused by gland compression and retraction, gland edema, and needle deflections can create significant areas of over dosage or under dosage to the gland [2]. There is a real need to decrease the complications associated with this modality of local therapy. For prostate brachytherapy, and other needle insertion tasks, the success rate of the procedure is directly related to the clinician's level of experience. Therefore, improvements in complication rates will be dependent on improving the training tools used by clinicians to improve the accuracy of needle guidance and for the case of prostate brachytherapy, accurate deployment of seeds within the prostate gland. Obtaining real world parameters for characterizing needle and tissue interaction is the first step towards developing a model to provide accurate haptic feedback in a training simulator for needle insertion tasks.

To date, a number of researchers have explored ways to improve surgeons' skills in procedures where little haptic and visual feedback exists. These mainly take the form of haptic simulators, for procedures such as catheter insertion [3], lumbar puncture [4], epidural blocks [5, 6], endoscopic surgeries, and laparoscopic surgeries. From the surgical simulation viewpoint, most tissue response modeling efforts in the literature are targeted towards assuming mechanical properties and developing methods to efficiently solve the tissue simulation problem for robot-assisted surgery/training. Several simulators have developed very sophisticated virtual environments that allow for plastic deformations of the material and interactions in multiple dimensions [7, 8]. However, it has been difficult to populate these models with data from real tissues.

For needle insertion tasks, needle experiments with modeling have been conducted by a number of researchers [6, 9-11]. However, most assume homogenous tissues, and no needle deflection. [6, 10-12] focused on needle insertion forces by quantifying the various forces involved during needle insertion. In this paper, we offer a different approach to obtaining the cutting force. Our method requires only one force sensor and we can internally image soft tissue movement during a needle insertion and withdrawal task.

Imaging modalities used during needle insertion into soft tissue have mainly been used for needle guidance. Our method of tracking internal markers using two C-arms facilitates the extraction of necessary parameters such as puncture force, cutting forces, and elastic modulus, required for accurate estimation of needle and soft tissue interaction. Fiducial tracking during needle insertion has been conducted by [9, 13], however their trials were conducted on transparent, homogeneous phantom tissues. To the author's knowledge, there has been no work on measuring in real time the 3-D movement of markers (beads) in non-homogeneous soft tissue

* This work was supported in part by National Science Foundation CAREER award IIS 0133471 and NSF ITR award 0312709.
Mr. James Hing is a graduate student in the PRISM laboratory (e-mail: jth23@coe.drexel.edu).
Dr. Ari D. Brooks is a General Surgeon specializing in Surgical Oncology at Drexel University College of Medicine (email: Ari.Brooks@DrexelMed.edu).
Dr. Jaydev P. Desai is the Director of the PRISM Laboratory, Drexel University, Philadelphia, PA 19104, USA (corresponding author, phone: 215-895-1738; fax: 215-895-1940; e-mail: desai@coe.drexel.edu).
[a] Corresponding author.

during needle insertion and we believe that our approach using two C-arms is novel. This type of reality based modeling is critical for providing accurate haptic feedback in surgical simulation.

This paper is divided into four sections. In section II, we discuss the materials and methods used for tracking implanted markers and the needle during an insertion and withdrawal task. Section III discusses the analysis of the image and force results and includes a discussion of our 3D finite element model. Section IV ends this paper with our conclusions and discussion of future work.

II. Materials and Methods

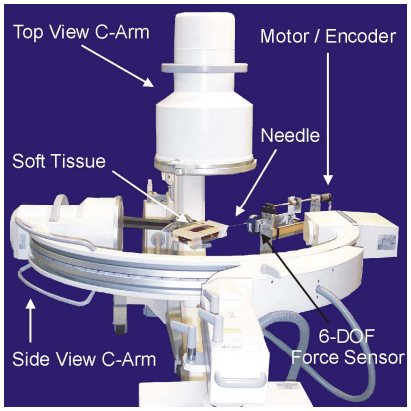

Fig. 1 Dual C-arm fluoroscope setup.

Dual C-arm fluoroscopes for bead tracking: Figure 1 shows the dual C-arm experimental setup for tracking the motion of beads inside the soft-tissue. To view the internal tissue movement during needle insertion and withdrawal, forty 1mm diameter stainless steel beads were inserted into the soft tissue. These beads were chosen because of their radiopacity (ability to block x-ray transmission) and their size, which was small enough to not affect the properties of the soft tissue or impede the needle insertion path. The beads were placed in a grid pattern spaced approximately 10mm apart from one another and in such a way to minimize occlusion between beads during imaging. Each bead was inserted perpendicular to the experiment needle path using an 18 gauge needle and to an approximate depth of 10 to 20mm from the tissue surface. Figure 2 shows the x-ray image of both the top and side view of the tissue sample before insertion (left) and during insertion (right). The OEC 7700 (side view) and OEC 9600 fluoroscopes (top view) were used to image implanted markers inside of the tissue and the needle during the experiments.

The C-arm's were positioned so that their imaging planes were orthogonal to each other, allowing for real time x-ray imaging of the side and top views of the implanted markers and needle tip during insertion. The video from each C-arm was captured onto a hard disk using a video capture device (Pinnacle Systems) at 29.97 frames per second and a resolution of 720 x 480 pixels.

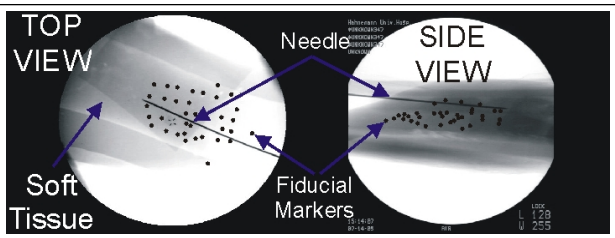

Fig. 2 Images acquired from both C-ARMs during needle insertion and withdrawal.(Markers enhanced for clarity)

Needle insertion device and tissue constraint: The needle apparatus was designed to measure the forces on a surgical needle during insertion into soft tissue. Figure 3 is a close up view of the needle insertion device and tissue constraint. A proportional derivative controller was used to achieve a constant velocity of 1.016mm/sec, 12.7mm/sec and 25.4mm/sec of the needle during insertion and withdrawal. The needle insertion device consists of a geared DC motor, an incremental encoder and a JR3 precision 6 axis force/torque sensor with 0.278 N accuracy and ±14 bit resolution. The needles used for the experiments were 18-gauge prostate seeding needles (Mick Radio Nuclear Instruments, Inc.) of length 20cm as shown in figure 4. This is consistent with the type of needle typically used by surgeons when performing prostate brachytherapy.

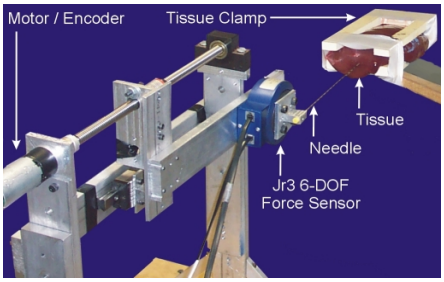

Fig. 3 Close-up of needle insertion apparatus

Based on our surgeon collaborations, liver consistency is very similar to the prostate and because the liver is easier to obtain and offers a larger workspace for quantifying the needle and soft tissue interactions, we chose to use porcine liver in our experiments. Three liver specimens were used and each specimen underwent five needle insertions at each speed of 1.016mm/sec, 12.7mm/sec and 25.4mm/sec.

The tissue samples were placed onto a flat plate and clamped such that the sides and back of the tissue were constrained from movement, leaving the front of the tissue free to move and unobstructed for needle insertion. To keep the setup as radiolucent (permits the penetration and passage of x-rays) as possible, the plate and clamp were made from machineable plastic and the clamp was held secure onto the tissue using surgical tape as seen in figure 3.

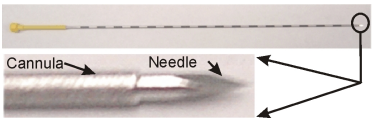

Fig. 4 Various components of a typical prostate brachytherapy seeding needle.

C-Arm calibration and marker registration: The quality of a C-arm image tends to suffer from two main causes of distortion: pincushion distortion and S curve distortion [14]. Pincushion distortion is caused from the mapping of a flat surface onto a curved input phosphor of the image intensifier (detector).

The S curve distortion is caused by the deflection of the electrons due to the earth's magnetic field and it is dependent on the angle of the image intensifier in the magnetic field. For each C-Arm used in the experiments, a calibration grid consisting of equally spaced patterned holes was imaged. Using Matlab, the centroids of the patterned holes were extracted. The pattern in the center of the image (within a 10 pixel window) is undistorted and the radial distance to the centroids of these holes from the center of the image was used as the "true" distance. As the distance from the center of the image to the centroids of the holes increase, there is significant variability between the "true" distance and the distorted image distance. A second order polynomial equation was fit to the error between the true distance to the centroids and distorted image distance.

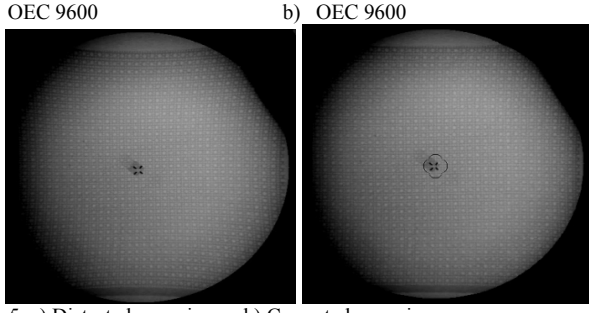

Fig 5. a) Distorted x-ray image b) Corrected x-ray image

Applying the polynomial to the distorted image (figure 5a):

$$\text{OEC 9600:} \quad y = 0.0006r^2 - 0.0706r + 1.6171 \qquad (1)$$
$$\text{OEC 7700:} \quad y = 0.0002r^2 - 0.0175r + 0.5651 \qquad (2)$$

(where y is the error in pixels between the correct and distorted position and r is the radial distance of the distorted point from the center of the image) corrected the distortion as shown in figure 5b. Each C-arm required separate polynomial corrections (equations (1) and (2) for C-arm fluoroscope model OEC 9600 and OEC 7700 respectively).

Magnification of points in the image also had to be considered. Magnification calibration for the two C-arms was conducted by imaging a radio-opaque ruler at various distances from the x-ray source. For each C-arm, the pixel to mm conversion as distance from the x-ray detector increased was fit with a second order polynomial where y is the number of pixels per mm and x is marker distance from the source in cm:

$$\text{OEC 9600:} \quad y = 0.00078402x^2 - 0.1093x + 5.5858 \qquad (3)$$
$$\text{OEC 7700:} \quad y = 0.00050624x^2 - 0.091541x + 6.0893 \qquad (4)$$

Correlation of a marker in the top view image with its location in the side view is obtained using the C-arm ability to continually image as it is rotated from 90 (top view) to 180 degrees (side view). During the rotation, each marker was tracked as it moved in the image from the top view to the side view. This was done before inserting the needle for each soft tissue sample.

After marker registration, the needle was moved into place and inserted approximately 90mm into the soft tissue at insertion speeds of 1.016mm/sec, 12.7mm/sec and 25.4mm/sec. During needle insertion, the JR3 force sensor captured the forces acting on the needle at 1000Hz while the side and top view C-arms continually recorded x-ray images of the needle position and the movement of the markers inside the tissue. After each insertion, the needle was moved to a different position in the soft tissue to minimize the chance of following a previous insertion path.

MATLAB image processing toolbox combined with standard kinematic transformations was used to extract the marker and needle coordinates in the global frame from the top and side view x-ray images. An image difference algorithm was applied from an image of the soft tissue with no beads to the frame being analyzed. This eliminated the outside boundaries of the images and highlighted only the marker and needle movement between the frames.

III. Results and Discussion

A. *Needle and Marker Movement*

Imaging the internal tissue movement is valuable for validating model results and quantifying tissue and needle interaction inside the tissue specimen.

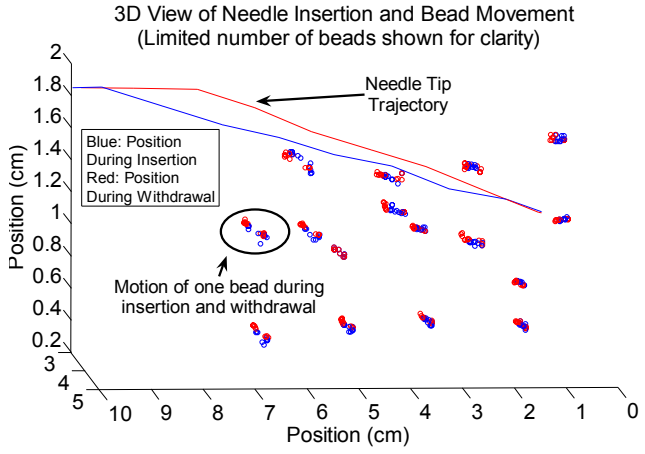

Figure 6. 3-D bead movement during needle insertion and withdrawal.

Figure 6 shows the extraction of the position of the internal markers and needle tip during an insertion experiment. As seen from the figure, there is significant movement of the bead during insertion and withdrawal of the needle in the tissue. While the movement is of the order of 1cm, this is significant since it would represent a large motion as compared to the size of the prostate (typically 40cm^3) and the proximity of the urethra, rectum, and bladder to an implanted radioactive seed in the prostate.

During withdrawal, to identify the start of the friction force on the needle, we took the following approach. At the start of withdrawing the needle, the needle does not slide inside the tissue but pulls the tissue in the direction of withdrawal until a force threshold to overcome the static friction and clamping force is reached. After this point, the needle begins to slide inside the tissue and kinetic friction begins. In our experiments we tracked the internal markers and needle movement in the C-arm videos. The time at which the relative velocity of the local internal markers with respect to the needle was no longer zero (corresponding to the moment when the needle is no longer dragging the tissue but is sliding past it) was identified as the start of kinetic friction during withdrawal.

The moment that tissue puncture occurs was found by following a similar approach during insertion of the needle. In our experiments with the C-arms, the relative velocities of the markers close to the needle insertion site are tracked along with the needle tip. The time at which the relative velocity of the marker with respect to the needle is no longer zero, can be taken as the time of puncture. There are two puncture events of the tissue which occur on the surface. A puncture event comprises of initial deformation of the tissue (leading to a rise in the force reading and movement of the local beads) followed by puncture (sudden drop in the force reading and a change in velocity of the local beads). The two puncture events are due to the fact that the needle tip and cannula do not have a seamless boundary (figure 4) (the first puncture occurs when the needle tip penetrates the surface of the tissue and the second puncture occurs when the cannula punctures through the surface). The second puncture is used in this study as the significant parameter because it is after the second puncture that the needle can be considered inserted into the tissue.

Table 1 (Mean Puncture force for each speed)

Speed	1.016mm/s	12.7mm/s	25.4mm/s
Liver 1	0.7063 N	0.5228 N	0.5881 N
± stdev	±0.1447	±0.1422 N	±0.1182 N
Liver 2	0.5196 N	0.5018 N	0.4979 N
± stdev	±0.2047 N	±0.1030 N	±0.0849 N
Liver 3	0.9424 N	0.5889 N	0.4967 N
± stdev	±0.1966 N	±0.1303 N	±0.1080 N
Mean Puncture (all Samples)	0.7228 N	0.5378N	0.5276 N
± stdev	±0.2471 N	±0.1231N	±0.1065N

Table 1 shows the mean force at the moment of puncture for each liver at various insertion speeds. As seen from the table, the mean puncture force for each liver sample is within one standard deviation of each other. Table 1 also shows that as the speed increases, the mean puncture force decreases, however the values are still within one standard deviation of each other.

Various internal puncture events can be identified by following the marker movement as the needle progresses inside the tissue. When local markers around the needle move with the same velocity as the needle tip, we can conclude that the needle is no longer cutting the tissue but is compressing it until puncture occurs and the relative velocities change.

B. Needle-Soft tissue interaction forces

Needle insertion consists of 4 events: initial puncture, insertion, relaxation, and withdrawal. Figure 7 shows the force data during an experimental needle insertion and withdrawal task. As the needle inserts farther into the soft tissue, it undergoes a series of major and micro punctures where the force rises and drops. Areas of significant changes in stiffness or obstacles inside the tissue result in major puncture events where the tissue is deformed at the same rate as the velocity of the needle tip until cutting occurs. Outside of these puncture events, the force increases relatively linearly during insertion due to the increase in friction as the surface area of the needle inside the tissue increases. Expanding on our previous work [15], we focused on quantifying the cutting force during needle insertion into soft tissue, and obtaining the local effective modulus of the tissue during the initial needle puncture of the tissue surface. Each of these values is important towards accurate simulation of a complete needle insertion and withdrawal task.

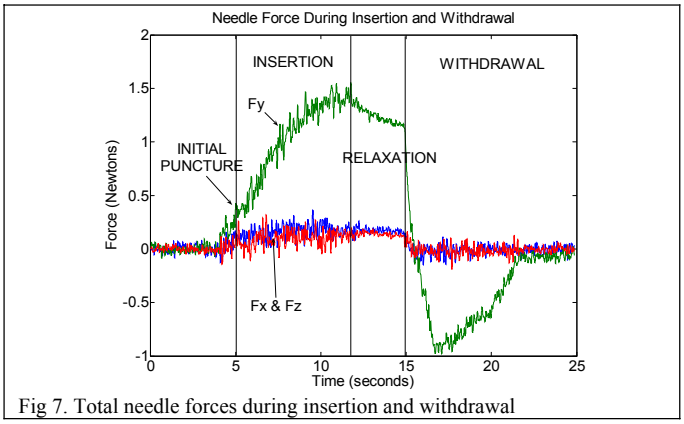

Fig 7. Total needle forces during insertion and withdrawal

Friction and cutting are major forces acting in the direction of insertion; therefore, the cutting force can be approximated by subtracting the force of friction from the total insertion force[11]. Friction force is approximated during withdrawal since the needle is no longer cutting the tissue. The needle does not start sliding within the tissue until the maximum force is reached during withdrawal. This is verified by image analysis described in the previous section.

Cutting force data can also be used to approximate the puncture force by using puncture force as the point where the

total insertion force data reaches the approximate cutting force data (see figure 8). This approximation correlates very well with the time of puncture obtained from image analysis. Alternatively, if the force data does not contain much noise and the puncture is significant, the puncture force can be seen as the point at which the force suddenly drops after rising, signifying the compression of the tissue and then quick release of the compression right after puncture.

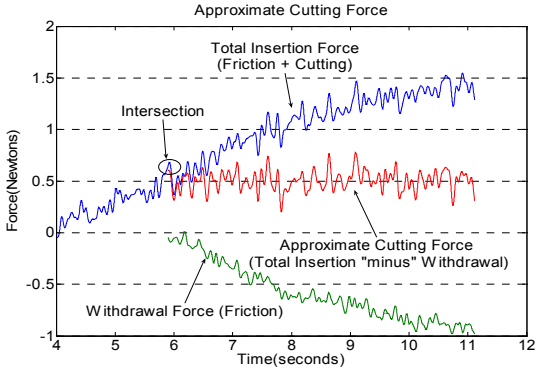

Fig 8. Plot of the approximate cutting force during needle insertion

. Figures 7 and 8 illustrate this approach with one needle insertion and withdrawal sample. When obtaining the approximate cutting force, the force from the relaxation phase and a portion of the withdrawal phase are not used. These sections of the graph do not correspond to the force of kinetic friction.

The approximate cutting force for puncture was obtained for each of the 45 insertions (3 livers*5 insertions*3 speeds). Using data from figure 8 as an example, the approximate cutting force varies around a single force value throughout the insertion, illustrating that the force required to cut through the tissue is fairly constant throughout the specimen. Table 2 below shows the mean approximate cutting force obtained from 15 insertions at each cutting speed.

Table 2 (Mean Cutting force for each insertion speed)

Speed	1.016mm/s	12.7mm/s	25.4mm/s
Liver 1	0.2978 N	0.4693 N	0.5643 N
± stdev	±0.0204 N	±0.1052 N	±0.1576 N
Liver 2	0.2109 N	0.4393 N	0.3794 N
± stdev	±0.1659 N	±0.1266 N	±0.0511 N
Liver 3	0.5613 N	0.4766 N	0.3819 N
± stdev	±0.0556 N	±0.0493N	±0.1223 N
Mean Puncture (all Samples)	0.3567 N	0.4618 N	0.4419 N
± stdev	±0.1807 N	±0.0933 N	±0.1420 N

The mean cutting force for 1.016mm/sec insertions tended to be lower than the cutting forces at faster speeds. However, the cutting force for each one of the 45 needle insertion and withdrawals had a much greater variation around the mean cutting value as the insertion speed decreased. The average variation around the mean cutting force was 0.1276N, 0.1454N and 0.3233N for each one of the 15 insertions at speeds of 25.4, 12.7, and 1.016mm/sec respectively. Less variation demonstrates that cutting was smoother for faster insertion speeds, and the needle was less prone to experiencing major puncture events inside the tissue.

C. *Modeling Needle Puncture*

A 3D model of the liver samples was built using ABAQUS (Version 6.3) software. As an initial approach, the model contains a global mesh of 0.5 x 0.5 x 0.5 cm^3, 8-node, solid linear brick elements with incompatible modes. The mesh is refined in the area of needle insertion to a size of 0.05 x 0.05 x 0.05cm^3. This allows for the needle tip to be represented by a 1mm^2 section of nine nodes. The actual 18 gauge needle has a diameter of 1.27mm. To reduce the computational load, the model was reduced to half the length of the typical tissue sample size (10cm) used in the experiments. After an analysis using a full size model, it was found that the stresses far away from the needle insertion point (past half length) were negligible (as expected by the Von Mises Criteria). The model was constrained so that it mimicked the experimental setup. The top and bottom side edges as well as the top and bottom back edges were fixed in all directions, leaving the front, side and back faces free to distort. The nine nodes representing the needle tip are displaced by the distance leading up to puncture and the local effective modulus is calculated following the procedure below. The wire model shown in Figure 9 a) shows the global mesh and the refined mesh located at the needle insertion site. Figure 9 b) shows how the model is deformed during an initial puncture and the stresses are computed based on the computed local effective modulus.

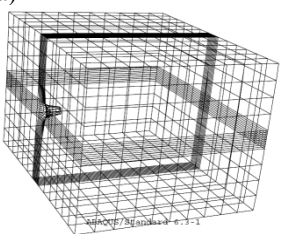

Fig. 9 a)3D FEM Wire Model

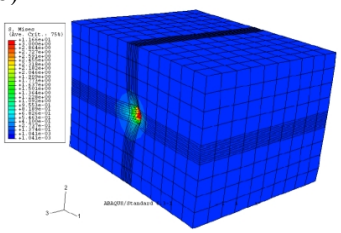

Fig. 9 b) 3D FEM Solid Model during puncture

Using the experimental puncture force obtained for each insertion and the amount of tissue movement, a finite element parametric study was conducted to obtain the local effective modulus for the initial needle puncture. The linear elastic, quasi-static, FEM analysis used a Poisson's ratio of 0.499 and an initial local effective modulus of arbitrary magnitude E_1. For each puncture, the nine needle nodes were given an experimentally measured displacement ΔU^{exp}. The computed change in force, ΔF^{FEM}, from the displacement at the nodes (ΔF^{FEM} is the forces at the nine needle nodes summed together) was compared with the change in force, ΔF^{EXP}, measured experimentally. Iterations were performed, each time modifying E_1 based on the value before until the error between ΔF^{FEM} and ΔF^{EXP} was within 1%. The final E_1 value

determined is the local effective modulus of the tissue during the puncture. Each puncture study reached the final E_1 value within 3 iterations.

Table 3 shows the mean E_1 value obtained for each of the three liver samples at various insertion speeds. The local effective modulus is fairly constant throughout each insertion speed and liver specimens indicating that there is little change in the properties of the tissue during the initial puncture at different speeds and between tissue specimens. This may be due to the small surface area of the needle deforming the tissue compared to the size of the specimen.

Also shown in table 3 are the mean LEM values for each insertion speed. The local effective modulus is used in the FEM model to obtain the local stresses and strains of the soft tissue during needle puncture.

Table 3 (Mean LEM value for each insertion speed)

Speed	1.016mm/s	12.7mm/s	25.4mm/s
Liver 1	14,345 N/m^2	14,014 N/m^2	16,874 N/m^2
± stdev	±2,735 N/m^2	±4,622 N/m^2	±3,119 N/m^2
Liver 2	12,558 N/m^2	16,558 N/m^2	13,403 N/m^2
± stdev	±4,482 N/m^2	±3,044 N/m^2	±2,194 N/m^2
Liver 3	17,246 N/m^2	14,203 N/m^2	11,632 N/m^2
± stdev	±4,663 N/m^2	±3,977 N/m^2	±3,030N/m^2
Mean Puncture (all Samples)	14,716 N/m^2	14,925 N/m^2	13,970 N/m^2
± stdev	±4,330.3 N/m^2	±3,866 N/m^2	±3,564 N/m^2

IV. Conclusion and Future Work

In this work, we studied needle and tissue interactions during a needle insertion and withdrawal task. Using a dual C-arm fluoroscope setup and implanted radio-opaque markers, we can extract the internal tissue motion during the insertion and withdrawal of a needle. Information such as the force and time of tissue puncture, various internal puncture events, and the start of kinetic friction during withdrawal can be extracted from the x-ray images by tracking the relative velocities of the implanted markers with the tip of the needle. Utilizing this image information along with the force information is one possible approach to finding the local effective modulus at various internal puncture events throughout the tissue. The approximate cutting force was found by subtraction of the total insertion force from the friction force. This cutting force can be used to characterize how much energy is required to cut at any location within the tissue.

Future work will require a closer evaluation of the deformation of the surface of the tissue near the needle insertion point as well as further analysis of the needle and tissue interactions farther into the tissue. The three dimensional FEM model will be further refined in locations of the coordinates of the implanted markers. A node located at the marker coordinate will represent that marker in the FEM model. The three dimensional movement of the implanted markers during needle insertion will be used to validate and modify our reality based finite element model which will be used in the development of a reality-based simulator for training radiation oncologists in prostate brachytherapy.

Acknowledgements

We would like to thank Dr. Justin Chandler and Jeff Justin for their valuable help in conducting dual C-ARM experiments and fluoroscope calibrations.

References

[1] A. Jemal, "Cancer Statistics," *CA Cancer J. Clin*, vol. 54, pp. 8-29, 2004.
[2] F. A. Vicini, V. R. Kini, G. Edmundson, G. S. Gustafson, J. Stromberg, and A. Martinez, "A comprehensive review of prostate cancer brachytherapy: defining an optimal technique," *International Journal of Radiation Oncology Biology and Physics*, vol. 44, pp. 483-491, 1999.
[3] E. Gobbetti, "Catheter Insertion Simulation with Co-registered Direct Volume Rendering and Haptic Feedback," *Medicine Meets Virtual Reality*, pp. 96-98, 2000.
[4] P. Gorman, "A Prototype Haptic Lumbar Puncture Simulator," *Proceedings of Medicine Meets Virtual Reality*, pp. 106-109, 2000.
[5] L. Hiemenz, "A Physiologically Valid Simulator for Training Residents to Perform an Epidural Block," *Proceedings of the IEEE Biomedical Engineering Conference*, pp. 170-173, 1996.
[6] P. N. Brett, A. J. Harrison, and T. A. Thomas, "Schemes for the Identification of Tissue Types and Boundaries at the Tool Point for Surgical Needles," *IEEE Transactions on Information Technology in Biomedicine*, pp. 30-36, 2000.
[7] G. Picinbono, H. Delingette, and N. Ayache, "Nonlinear and anisotropic elastic soft tissue models for medical simulation," presented at IEEE International Conference on Robotics and Automation, 2001.
[8] C. Forest, H. Delingette, and N. Ayache, "Cutting Simulation of Manifold Volumetric Meshes," *Proceedings of the Fifth International Conference on Medical Image Computing and Computer Assisted Intervention*, vol. 2, pp. 235-244, 2002.
[9] S. P. DiMaio and S. Salcudean, "Needle insertion modeling and simulation," presented at IEEE International Conference on Robotics and Automation, 2002.
[10] H. Kataoka, T. Washio, K. Chinzei, K. Mizuhara, C. Simone, and A. Okamura, "Measurement of Tip and Friction Force Acting on a Needle During Penetration," *Proceedings of the Fifth International Conference on Medical Image Computing and Computer Assisted Intervention*, pp. 216-223, 2002.
[11] C. Simone, "Modeling of Needle Insertion Forces for Percutaneous Therapies," in *Department of Mechanical Engineering*. Baltimore, MD: The Johns Hopkins University, 2002.
[12] M. Heverly, P. Dupont, and J. Triedman, "Trajectory optimization for dynamic needle insertion," presented at IEEE International Conference on Robotics and Automation, Barcelona, Spain, 2005.
[13] J. Crouch, C. Schneider, J. Wainer, and A. Okamura, "A velocity dependent model for needle insertion in soft tissue," presented at MICCAI, Palm Springs, CA, 2005.
[14] W. Hendee and E. Ritenour, "Fluoroscopy," in *Medical Imaging Physics*: Wiley, 2002, pp. 235 - 250.
[15] J. Hing, A. Brooks, and J. P. Desai, "Reality-based estimation of Needle and Soft-tissue interaction for accurate haptic feedback in prostate brachytherapy simulation," presented at International Symposium of Robotics Research, San Francisco, CA, 2005.